Supplementary Materials for

Tailoring Vibrational Excitation Pathways for High-Yield Oxidation of Methane to Methanol

Charan R. Nallapareddy, Thomas C. Underwood*

*Corresponding author. Email: thomas.underwood@utexas.edu

This PDF file includes:

Supplementary Text
Figs. S1 to S22
Tables S1 to S3
Reference

Supplementary Text

1A. Selectivity-conversion limit: Three step kinetic model

In this section, we show the derivation for the selectivity – conversion limit of methane partial oxidation to methanol. We use a reduced-order kinetic model with first-order dependence on the reactants.

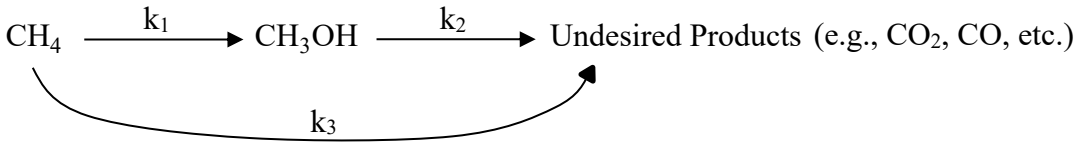

In this framework, the rate of methane consumption, $\frac{dp_{CH4}}{dt} = -k_1 p_{CH4} - k_3 p_{CH4}$, can be solved to give,

$$\Rightarrow \qquad p_{CH4} = p_{CH4_0} \exp\left(-(k_1 + k_3)t\right); \qquad \text{Conversion} = 1 - \exp\left(-(k_1 + k_3)t\right), \qquad \text{(A1)}$$

where p_{CH4_0} is the initial methane partial pressure, and k_1, k_2 and k_3 are rate constants that are described in the main text. Backward reactions are neglected due to the relative stability of the products and reactants (i.e., products are more stable than reactants). The rate constants are approximated as being time independent as the variations in gas temperature and pressure during conversion are small.

The rate of methanol production, $\frac{dp_{CH3OH}}{dt} = k_1 p_{CH4} - k_2 p_{CH3OH}$, can also be solved,

$$\frac{dp_{CH3OH}}{dt} + k_2 p_{CH3OH} = k_1 p_{CH4} = k_1 p_{CH4_0} \exp(-(k_1 + k_3)t),$$

where (A1) was substituted for p_{CH4}. In the limit there is no methanol in the reactor initially, the partial pressure of methanol can be solved,

$$p_{CH3OH} = \frac{p_{CH4_0} k_1}{k_2 - (k_1 + k_3)} \left(\exp(-(k_1 + k_3)t) - \exp(-k_2 t)\right).$$

If $k_1 + k_3 = k$ is substituted, the yield of methanol can be expressed as,

$$\Rightarrow \qquad \frac{k_1}{k_2 - (k_1 + k_3)} = \frac{k}{k_2 - k}\left(\frac{k_1}{k}\right) = \frac{ak}{k_2 - k} = A,$$

$$\Rightarrow \qquad \text{Yield} = \frac{p_{CH3OH}}{p_{CH4}} = A\left(\exp(-kt) - \exp(-k_2 t)\right).$$

1B. Breaking selectivity-conversion limit: Modified kinetic model

In this section, we show the modified kinetic model with first-order dependence on the reactants to accommodate active removal process (Fig. 4).

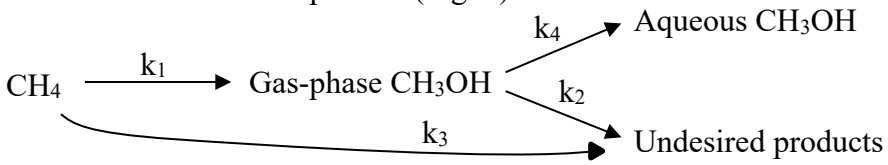

As explained in Sec. 1A, reactions are neglected and rate constants are treated as being constant in time.
Similar to the three-step model,

$$\Rightarrow \qquad p_{CH4} = p_{CH4_0} \exp\left(-(k_1 + k_3)t\right); \qquad \text{Conversion} = 1 - \exp\left(-(k_1 + k_3)t\right). \qquad \text{(A2)}$$

A reaction transport model describes the generation of CH_3OH in the gaseous phase and its motion throughout the reactor. In the limit where CH_3OH is captured in another phase (i.e., water) that is static (CH_3OH_w), a separate reaction model describes its accumulation,

$$\frac{\partial c_{CH_3OH_g}}{\partial t} = \nabla\cdot(D\nabla c_{CH_3OH_g}) - \nabla\cdot(\mathbf{v} c_{CH_3OH_g}) + R_1,$$

$$\frac{\partial c_{CH_3OH_w}}{\partial t} = R_2,$$

where D is the diffusion coefficient of CH_3OH_g, $\mathbf{v}$ is the mixing velocity of gas within the reactor, R_1 is the net rate of production of CH_3OH_g, and R_2 is the net rate of production of CH_3OH_w in the aqueous phase. If there is a large volume of water to trap CH_3OH, additional transport effects in the aqueous phase would need to be considered (i.e., diffusion or convection if mixing of the liquid phase occurs). The reaction transport model can be recast in terms of species partial pressures if the reaction is constrained to proceed at 1 atm and fixed temperature,

$$\frac{\partial p_{CH_3OH_g}}{\partial t} = \nabla\cdot(D\nabla p_{CH_3OH_g}) - \nabla\cdot(\mathbf{v} p_{CH_3OH_g}) + R_1.$$

In the limit where a pump is used to circulate reactants and products throughout the mixture, diffusive transport effects become negligible (i.e., characteristic timescales are much longer). Even without a pump, the addition of plasma energy in nanosecond pulses has been shown to generate shock waves that induce convective transport within the reactor (Fig. S8).

$$\frac{\partial p_{CH_3OH_g}}{\partial t} = -\nabla\cdot(\mathbf{v} p_{CH_3OH_g}) + R_1$$

Detailed insight into the production and spatial evolution of CH_3OH requires solving the details of the reaction transport equations in space and time for each species of interest. These models must incorporate reaction kinetics, transport models, and plasma fluid frameworks to quantify the energy distribution of electrons and characteristic reaction rates of intermediate states.

Instead, our focus in this paper is to validate mechanisms to extend high selectivity conversion of CH_4 into CH_3OH to high degrees of conversion. We thus focus on using a global kinetic framework to validate the temporal trends of CH_3OH that is partitioned in the gaseous and aqueous phases as plasma energy is deposited. To convert spatial transport effects, such as diffusion, into a time-dependent effect, we introduce a characteristic gradient length scale, L_∇, that

generates a convective flux of CH_3OH, and assume a characteristic mixing velocity, V_{mix}, that remains independent of space and time,

$$\frac{\partial p_{CH_3OH_g}}{\partial t} = - \nabla\cdot(\mathbf{v} p_{CH_3OH_g}) + R_1 \sim - \frac{1}{\mathbf{L_\nabla}} \mathbf{V_{mix}} p_{CH_3OH_g} + R_1$$

$$\frac{\partial p_{CH_3OH_g}}{\partial t} \sim - \frac{1}{\mathbf{L_\nabla}} \mathbf{V_{mix}} p_{CH_3OH_g} + R_1 = - \frac{1}{\mathbf{L_\nabla}} \mathbf{V_{mix}} p_{CH_3OH_g} + k_1 p_{CH4} - k_2 p_{CH3OH_g} - k_{CH3OH} p_{CH3OH_g}$$

$$\text{Let} \quad k_4 = k_{CH3OH} + \frac{1}{\mathbf{L_\nabla}} \mathbf{V_{mix}}$$

$$\frac{\partial p_{CH_3OH_g}}{\partial t} \sim k_1 p_{CH4} - k_2 p_{CH3OH_g} - k_4 p_{CH3OH_g}$$

$$\text{Boundary condition:} \quad \frac{\partial p_{CH_3OH_w}}{\partial t}\Big|_{interface} = k_4 p_{CH3OH_g}$$

Since the effective reactor residence timescale is in the order of minutes, it is sufficient to introduce turbulent mixing in the liquid phase. Therefore, one can treat the methanol concentration or partial pressure to be uniform in liquid phase. This implies,

$$p_{CH_3OH_w} = p_{CH_3OH_w}|_{interface}.$$

The rate of gaseous methanol production, $\frac{dp_{CH3OH_g}}{dt} = k_1 p_{CH4} - k_2 p_{CH3OH_g} - k_4 p_{CH3OH_g}$, can also be solved,

$$\frac{dp_{CH3OH_g}}{dt} + (k_2 + k_4) p_{CH3OH_g} = k_1 p_{CH4} = k_1 p_{CH4_0} \exp(-(k_1 + k_3)t),$$

$$p_{CH3OH_g} = \frac{p_{CH4_0} k_1}{(k_2 + k_4) - (k_1 + k_3)} \left(\exp(-(k_1 + k_3)t) - \exp\left(-(k_2 + k_4)t\right)\right).$$

The rate of aqueous methanol production, $\frac{dp_{CH3OH_w}}{dt} = k_4 p_{CH3OH_g}$, can also be solved,

$$p_{CH3OH_w} = \frac{p_{CH4_0} k_1 k_3}{(k_2 + k_4) - (k_1 + k_3)} \left((1 - \exp(-(k_1 + k_3)t)) \frac{1}{k_1 + k_3} - (1 - \exp(-(k_2 + k_4)t)) \frac{1}{k_2 + k_4} \right).$$

Since p_{CH3OH_g} is two orders of magnitude smaller than p_{CH3OH_w} (Fig. S1),

$$\text{Yield} = \frac{k_1 k_3}{(k_2 + k_4) - (k_1 + k_3)} \left((1 - \exp(-(k_1 + k_3)t)) \frac{1}{k_1 + k_3} - (1 - \exp(-(k_2 + k_4)t)) \frac{1}{k_2 + k_4} \right).$$

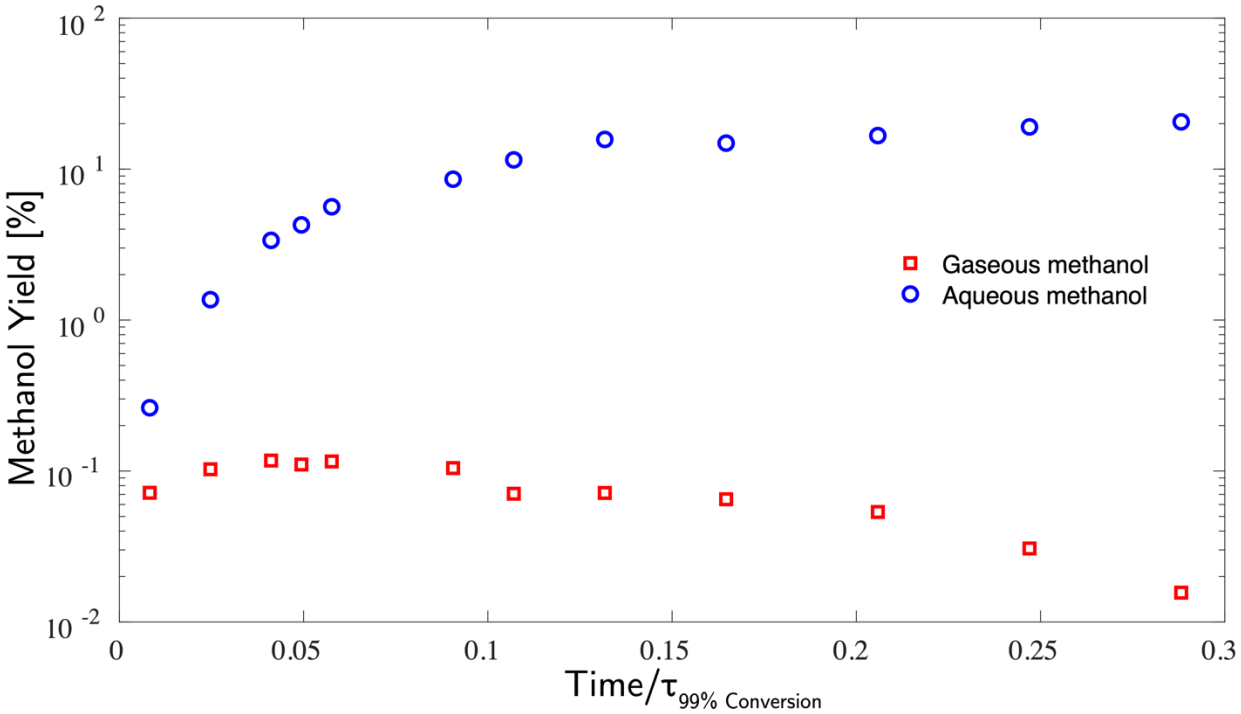

Fig. S1. Comparison of methanol yield partitioning between the gaseous and aqueous phases.

Measurements of product partitioning indicate that methanol is trapped preferentially in aqueous samples if it is purged continuously. The gaseous products were purged through 15 mL of water with up to 85 SCCM flow rate. The properties of the plasma discharge include a 1 cm discharge gap, applied voltage of ~ 9 kV and repetition frequency of 1 kHz. $\tau_{99\% \text{ Conversion}} = 5/(k_1+k_3)$.

2. Influence of inert gas

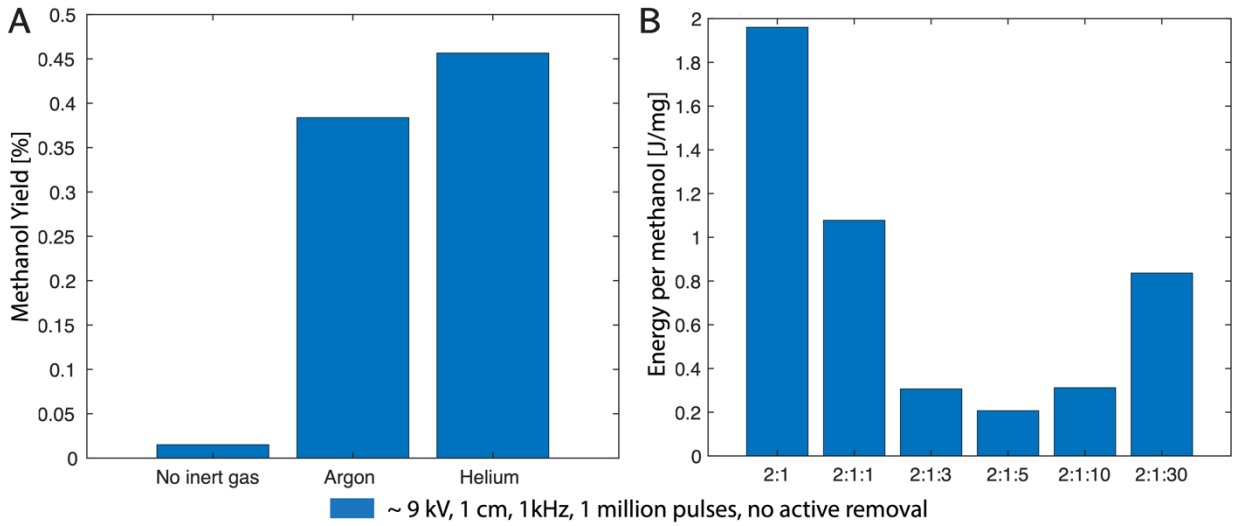

Fig. S2. Influence of inert gas on methanol selectivity.

(**A**) A comparison of different inert gases on the methanol yield. (**B**) Energy cost of methanol production. Argon at a concentration of CH_4: O_2: Ar = 2:1:5 (by volume) was found to be the most energy efficient.

An inert gas was added to the reactor to stabilize the plasma and to lower the reduced electric field (E/N) that was required to initiate a discharge. Together, these enabled higher yields of methanol. Argon was chosen as the inert gas as the methanol yield difference between argon and helium was small (Fig. S2A) and argon is more economic. Various inert gas compositions were also compared to choose a gas composition for the plasma reactor. A composition of 2:1:5 was used throughout the study to minimize energy costs (Fig. S2B).

3. Product composition at varying E/N

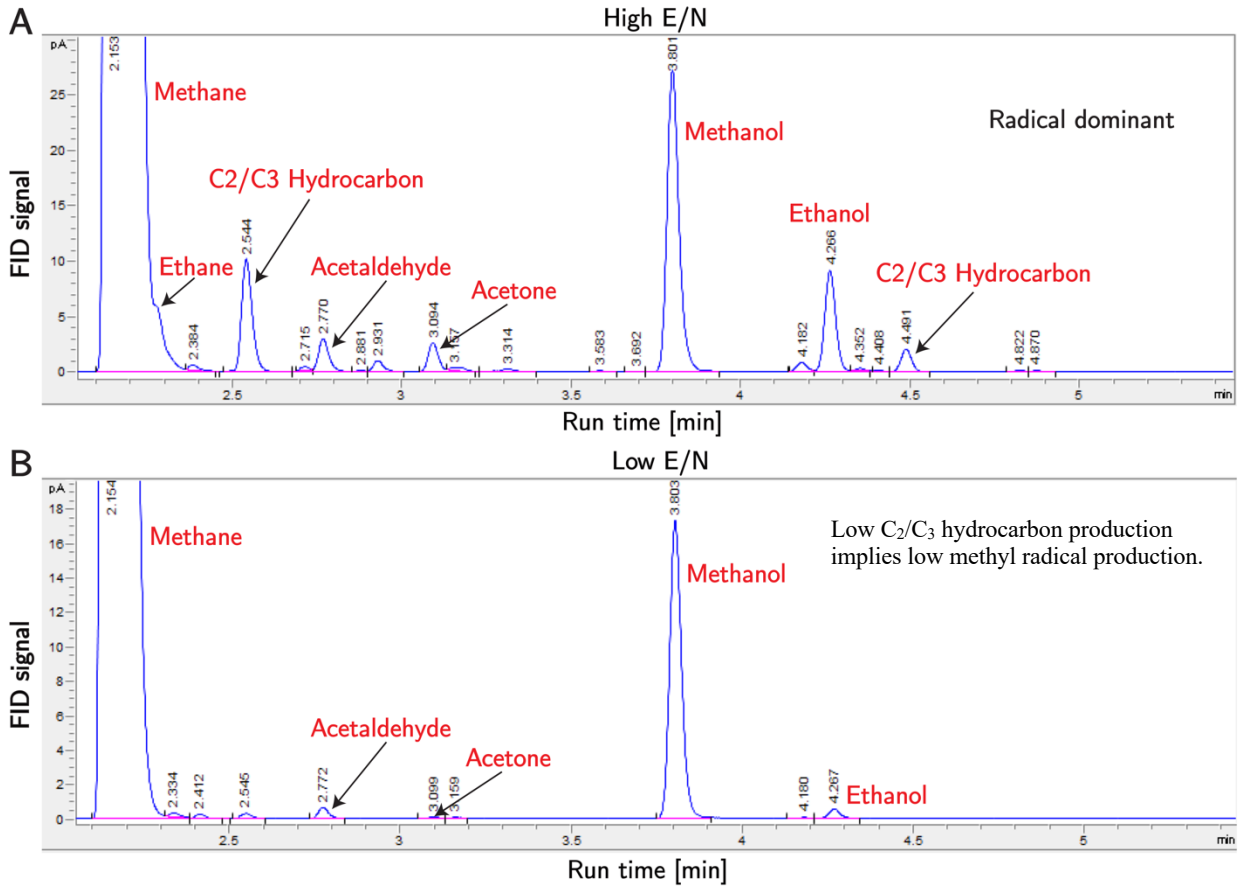

Fig. S3. Comparison of high E/N and low E/N FID signals to show that lowering E/N increases selectivity to methanol.
(**A**) GC-FID signal after exposure to a plasma with high E/N (spark, ~ 100 Td). Other reactor settings are reported in Fig. 3B. (**B**) GC-FID signal after exposure to a plasma with low E/N (diffused discharge, ~ 10 Td).

Increasing product selectivity toward methanol was observed as the E/N of the discharge reduced. Higher voltages (or shorter discharge gaps) were found to feature prominent C_2/C_3 hydrocarbons and less oxygenates in the GC FID product composition (Fig. S3A). As voltage was lowered (or discharge gaps were increased), product selectivity toward methanol was found to increase (Fig. S3B). Higher E/N increases the production of methyl radicals and the cascade of unwanted hydrocarbon products (Fig. 3 and Sec. 12).

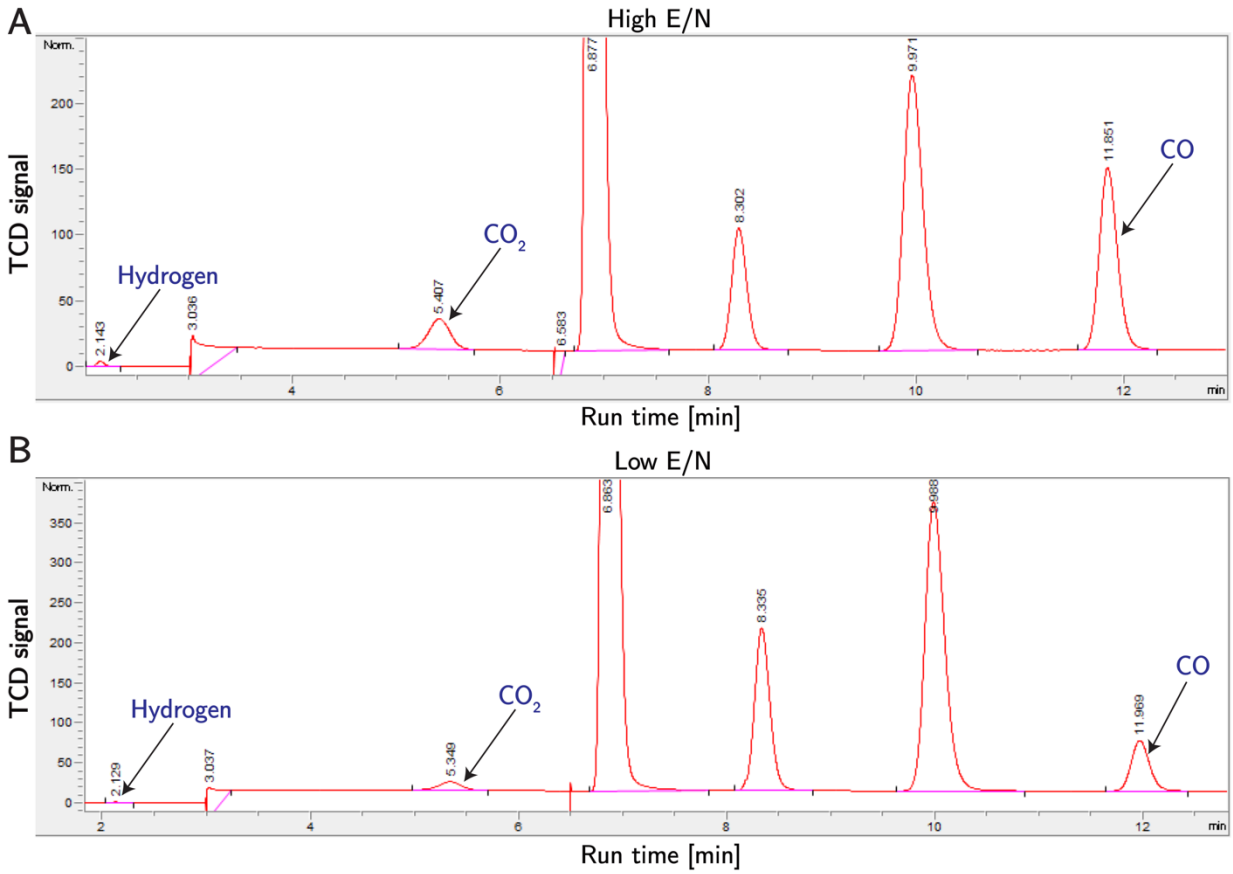

Fig. S4. Comparison of high E/N and low E/N TCD signals to show that low E/N results in less methanol over-oxidation.
(A) GC-TCD signal after exposure to a plasma with high E/N (spark, ~ 100 Td). Other reactor settings are reported in Fig. 3B. (**B**) GC-TCD signal after exposure to a plasma with low E/N (diffused discharge, ~ 10 Td).

Along with lower C_2/C_3 production (lower k_3), lower E/N resulted in lower CO_2 and CO production which indicates a higher selectivity to methanol.

To calculate the production rate of CH_3 in filamentary (T ~ 600K) and diffused (T ~ 300K) discharges, the following elementary step was considered,

$$CH_4(v) + O \rightarrow CH_3 + OH.$$

The rate coefficient corresponding to this reaction is,

$$k = 3.15\times10^{12}\ T^{0.5} \exp\left(-\frac{1.03\times10^{4} - E_v}{RT}\right).$$

The vibrational energy corresponding to CH_4 ($\nu_{2,4}$) ~ 1500 cm^{-1}.

k (T = 300K) = 2.32 x 10^9 cm^3/s; k (T = 600K) = 5.03 x 10^{11} cm^3/s

This implies that the flux toward CH_3 and OH in diffused mode = $\frac{k\,(300K)}{k\,(300K) + k\,(600K)} \times 100 = 0.46$ %

4. Plasma discharge regimes

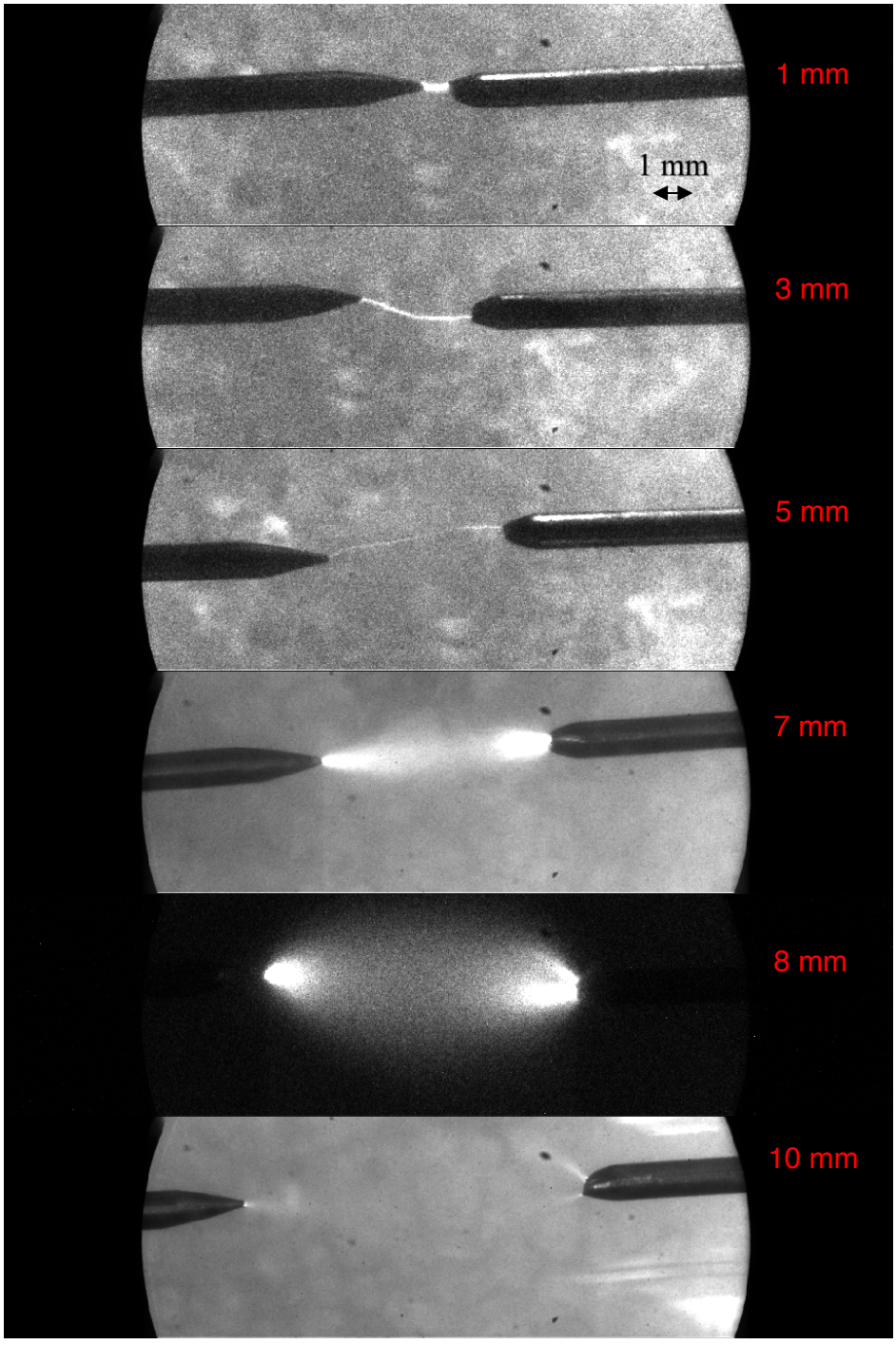

Fig. S5. Different regimes of nanosecond pulsed plasma discharges.
Intensified CCD images of a point to plane plasma discharge with varying gap distances (~9 kV, 1 kHz) and a fixed gaseous composition of CH_4:O_2:Ar = 2:1:5. For discharge gaps between 1-5 mm, the exposure time was 100 µs and gain was 200 (max 255). For discharge gaps between 7-10mm, the exposure time was 20 ms and gain was 220 to capture the fainter diffused discharge.

Experiments were performed to visualize the change in plasma structure (i.e., plasma regime) with varying E/N. Varying the applied voltage (Fig. 2) and the discharge gap (Fig. 3 and S6) were used to study these effects. Images of the plasma structure were recorded with discharge gaps between 1 mm and 1 cm. The plasma transforms from a filamentary discharge at smaller discharge gaps (high peak current ~ 2-3 A) to a more diffused plasma at higher discharge gaps (smaller peak current ~ 40 - 200 mA). For filamentary discharges (1mm – 5mm), a shorter exposure time (100 μs) and a gain setting of 200 were used, as the light output was large. For more diffused discharges (7mm – 10mm), a 20 ms exposure time was used with a gain setting of 220.

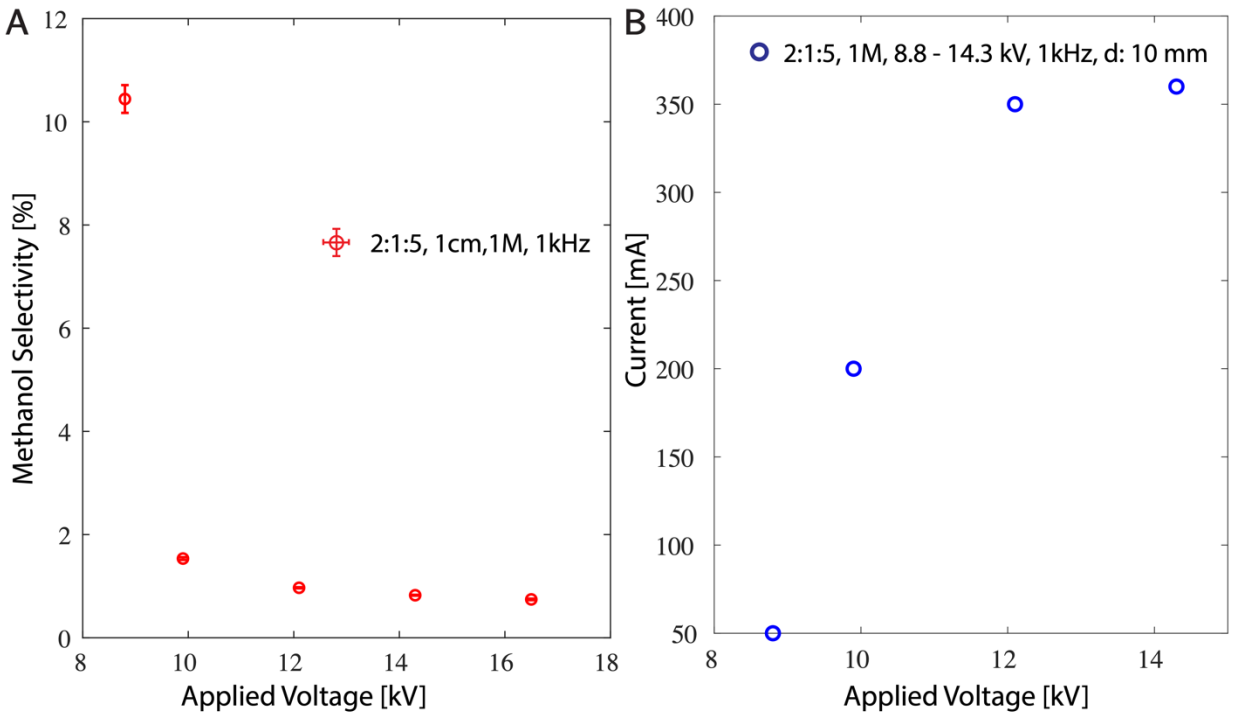

Fig. S6. Demonstration of the equivalence of varying voltage with constant discharge gap and varying discharge gap with constant voltage.

(**A**) Methanol selectivity lowers as applied voltage increases. This is how changing applied voltage in Fig. 2 showed difference in yield. (**B**) Discharge current increases with applied voltage. This implies increasing voltage induces a structural transition in the plasma as the discharge becomes more filamentary [1] and less selective to vibrational excitations.

5. Spatial invariance in the reactor

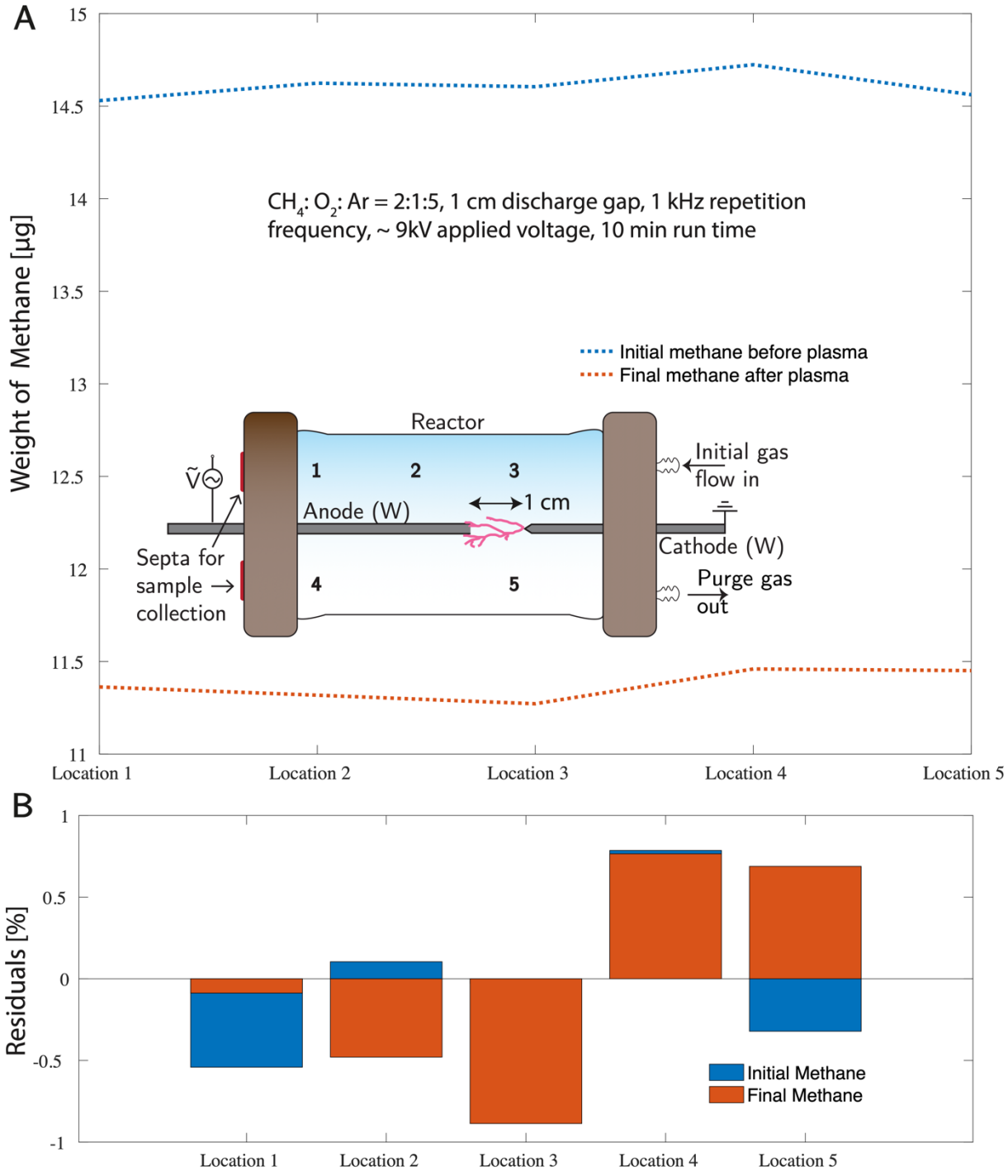

Fig. S7. A check for spatial homogeneity in the reactor.
(**A**) Sampling at five different locations in the reactor shows variation in sampling amount across locations. Initial methane refers to the amount of methane sampled from the reactor before the reaction. Final methane refers to the amount of methane sampled after the reaction. (**B**) The measured variation of methane composition was < 1% across all locations.

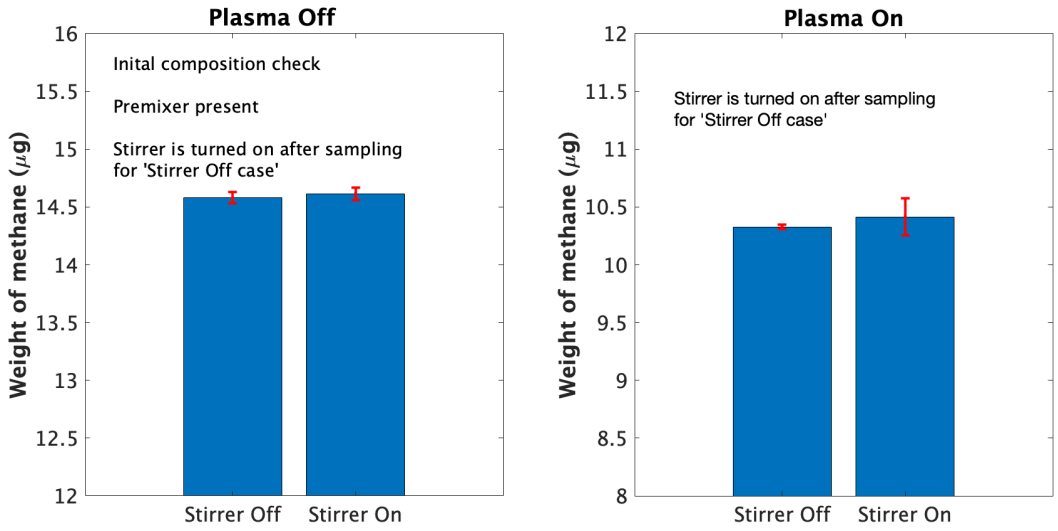

Fig. S8. A check for reactor mixing dependence on the stirrer.
(**A**) "Plasma Off " refers to the conditions before the chemical reaction (CH_4:O_2:Ar = 2:1:5). Turbulent flow generators were present upstream of the reactor and downstream of the mass flow controllers to mix methane, oxygen, and argon thoroughly before they enter the reactor. (**B**) "Plasma On" refers to the conditions after the chemical reaction (conditions same as Fig. S7).

Nanosecond pulsed plasmas generate shock waves and vortex rings that mix the contents of the reactor [2]. Measurements of methane concentration within the reactor indicate this eliminates the need for a stirrer (Fig. S8). In addition, to ensure spatial homogeneity, composition was checked at a few different locations and the uncertainty in the measurements are reported in Fig. S7. For initial composition mix (when plasma is not present), a premixer was used to make sure the composition entering the reactor is well-mixed beforehand (Fig. S8A).

6. Calibration curves

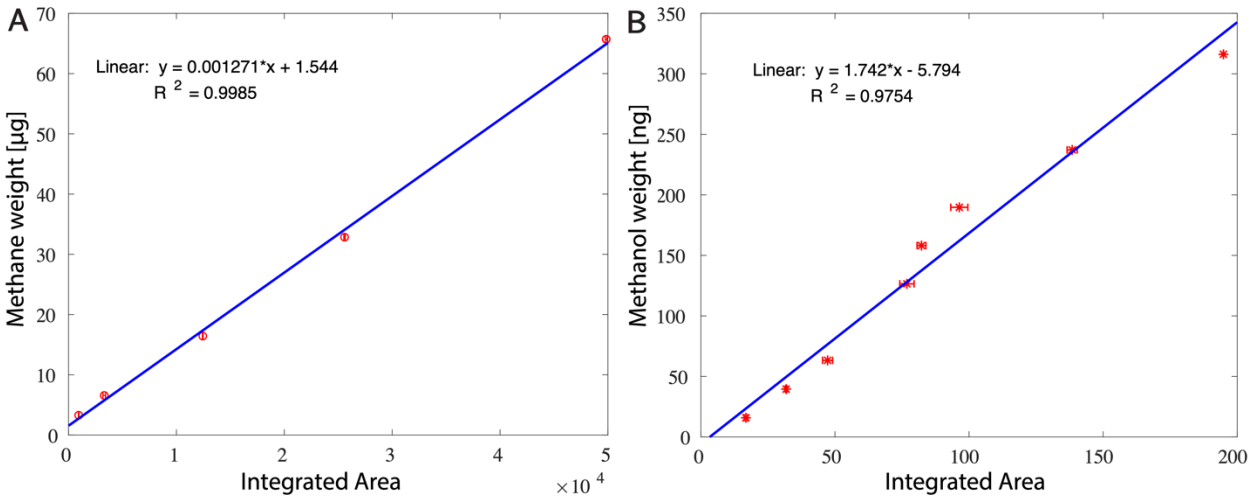

Fig. S9. Methane and methanol calibration curves.

(**A**) Methane calibration curve obtained with GC-FID and gas-tight syringes (Materials and Methods). (**B**) Methanol calibration curve obtained with GC-FID and a µl syringe (Materials and Methods).

7. Nuclear magnetic resonance (NMR)

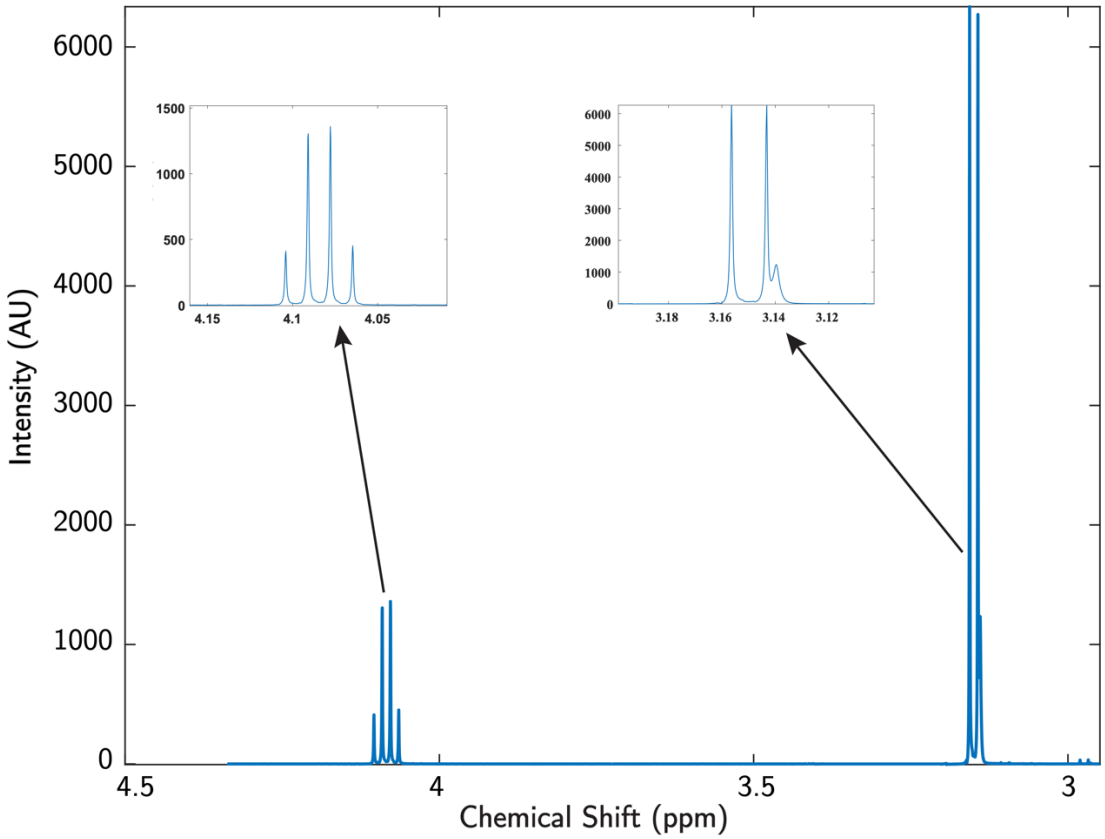

Fig. S10. A Bruker 600 MHz NMR spectrometer was used to obtain 1D ^{1}H-NMR spectrum of methanol generated in the plasma reactor (Number of scans: 32 and pulse width: 45°).

A Bruker 600 MHz NMR spectrometer was used to obtain a 1D ^{1}H-NMR spectrum (Fig. S10) of the reaction products dissolved in a cold aqueous sample (T ~ 4 °C) and validate the presence of methanol in the GC FID traces. Samples were prepared by bubbling contents of the 100 ml reactor vessel through a cold 1 ml aqueous sample. Quantitative analysis was performed by spiking the sample with Tetramethylsilane (NMR grade, > 99.9% purity, CAS: 75-76-3 from Millipore Sigma) for referencing and a known amount of Deuterated Chloroform ($CDCl_3$) and Deuterated Water (D_2O) for quantification of methanol using the quartet signal.

NMR was used to doubly confirm the presence of methanol in the product samples. As methanol was produced in the gas phase, GC-FID was used to detect and quantify methanol in gas phase. However, as NMR requires liquid samples, gas-phase components were first bubbled through 1 ml water to dissolve soluble products like methanol. Since methanol retention capacity of water is not 100%, the results obtained using NMR were only used to confirm the presence of methanol in GC measurements. However, qNMR yields were of the same order as GC-FID measurements.

8. Energy loss fractions

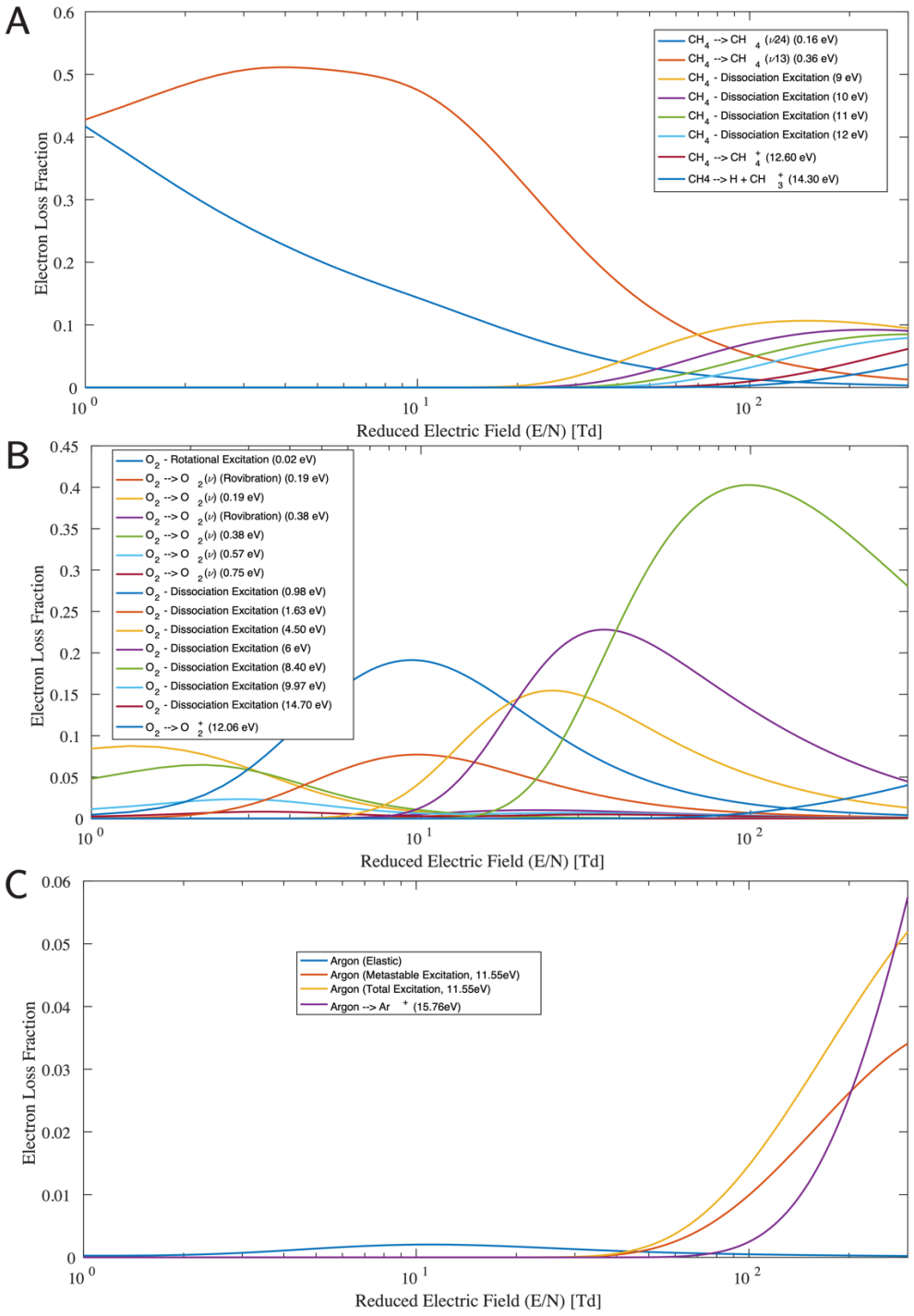

Fig. S11. Electron loss fractions of CH_4, O_2 and Ar with 2:1:5 composition at 300 K and 1 atm.

(A) Electron loss fractions of methane. (B) Electron loss fractions of oxygen using. (C) Electron loss fractions of argon. All the curves were obtained using Bolsig+ with settings described in Methods and Materials.

9. Methane vibrational levels and timescales

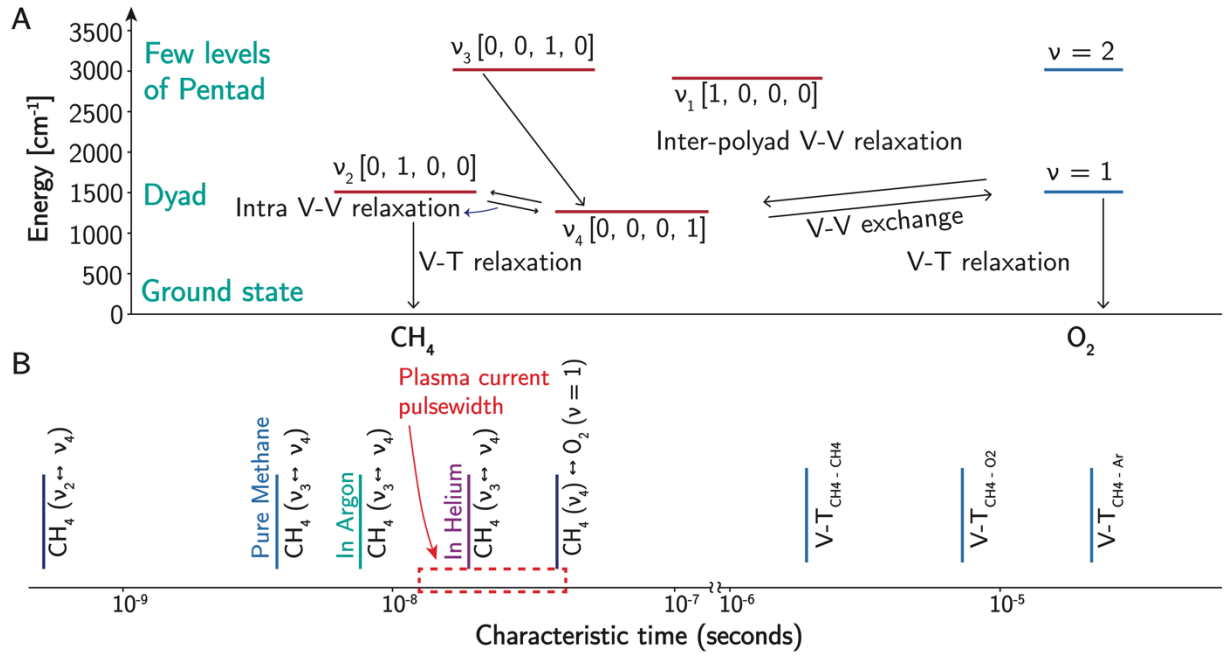

Fig. S12. Inter-molecule synergy between vibrational energy levels in CH_4-O_2 system and their relaxation timescales.

(A) Select vibrational levels of methane and oxygen to show vibrational – vibrational (V-V) and vibrational – translational (V-T) relaxations [3,4]. (B) Characteristic timescales of these relaxation processes [5–7].

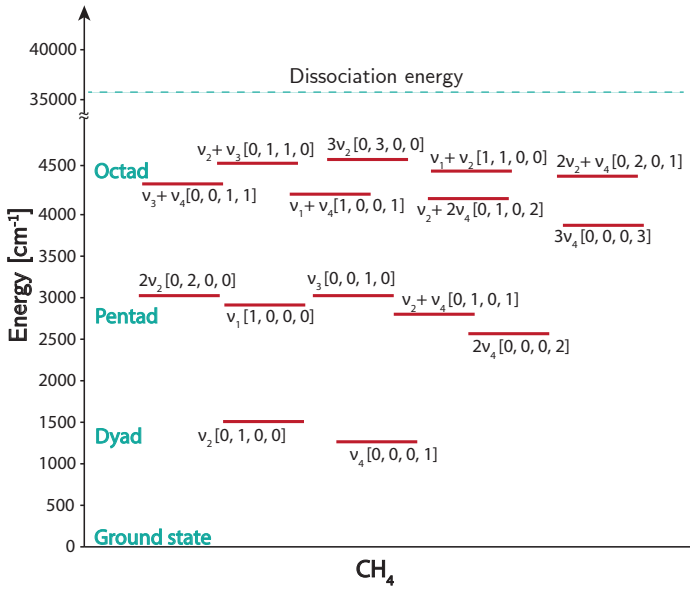

Fig. S13. The full complex vibrational and sub-vibrational levels of methane up to Octad.

10. Evaluating electrical energy costs per pulse

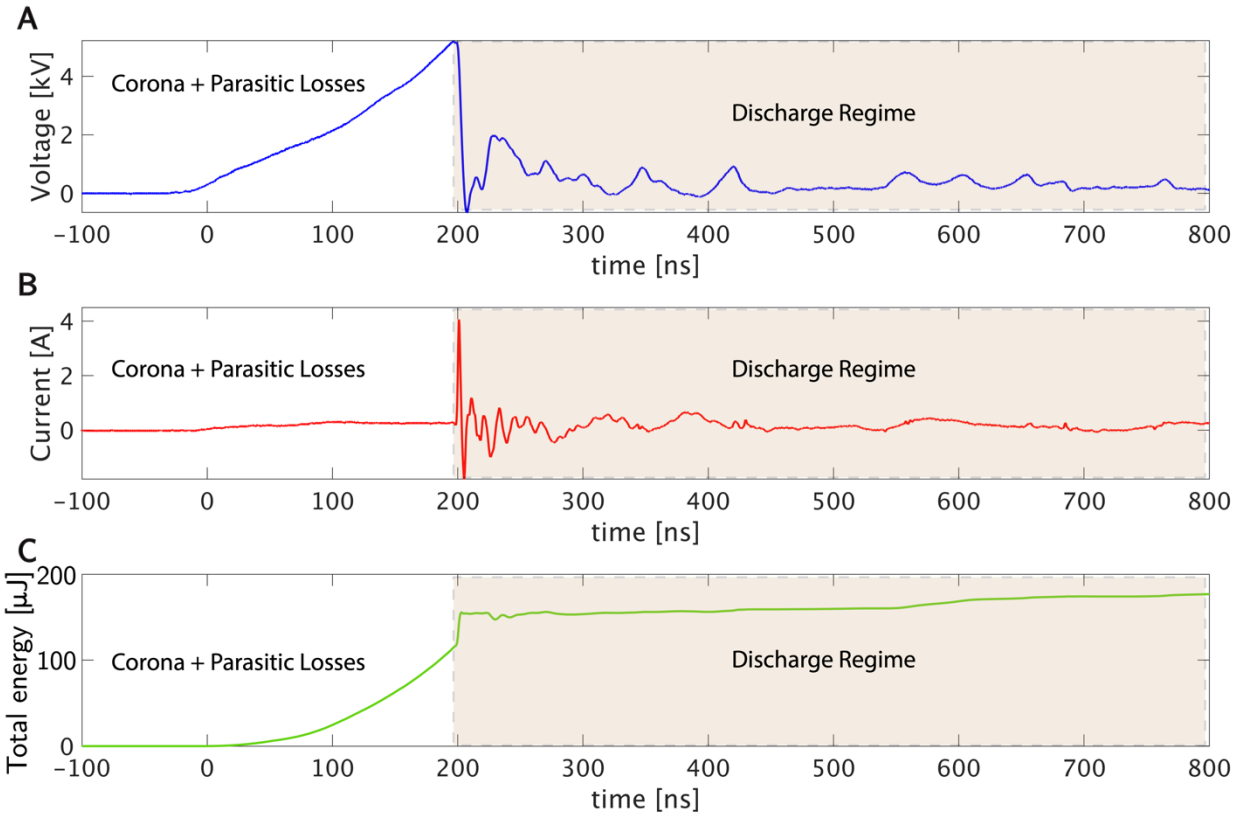

Fig. S14. Energy per pulse evaluation in the spark discharge regime.
(A) Voltage waveform for 1 mm discharge gap with initial corona phase (i.e., voltage rise period) and the spark discharge phase. (B) Current waveform showing the corona and spark regime. (C) Variation of energy with time during a pulse to show the energy consumption differences between the corona and spark phases.

The energy per pulse at discharge gaps ≤ 5 mm (i.e., in the spark regime) was determined initially by integrating the product of current and voltage. However, due to our nanosecond pulser's rise time of approximately 200 ns, a significant portion of the calculated energy was attributed to corona and parasitic losses (Fig. S14C). Much of this energy is not deposited to molecules within the reactor. In particular, corona discharges did not contribute to methane conversion or methanol yield (Fig. S16A). Based on these measurements, corona and parasitic losses were subtracted from the energy per pulse measurements to eliminate limitations of energy deposited by our pulser. Energy deposition toward the spark generation started from the moment when the voltage reached its peak value to approximately one microsecond, after which the deposited energy remained relatively constant (Fig. S14C).

For longer discharge gaps, plasma generation (diffused discharge) was not possible due to the additional load the voltage probe imposed on the plasma generation circuitry. Consequently, voltage waveforms at these longer discharge gaps could not be obtained which rendered the traditional method of calculating energy by integrating the product of current and voltage unusable.

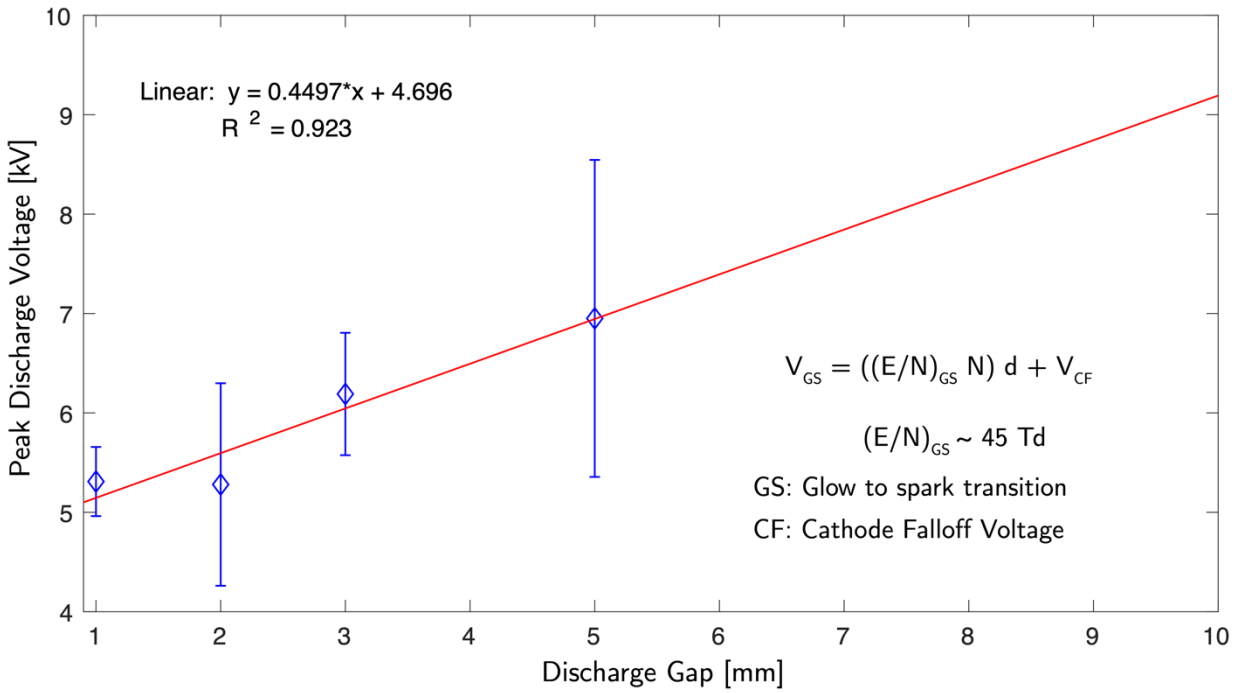

Fig. S15. Peak discharge voltage estimation at longer discharge gaps (> 5 mm). (A) Theoretical evaluation of peak discharge voltage at longer discharge gaps based on the transition voltage between the glow (i.e., diffused discharge) and spark regimes [8]. Error bars shown indicate standard deviation over 1000 measurements.

As obtaining voltage waveform for discharge gaps > 5 mm was not possible due to capacitive loading by the voltage probe, peak discharge voltage was estimated by fitting the data obtained at shorter discharge gaps using a theoretical glow to spark transition voltage fit from the literature [8] (Fig. S15). The estimated peak discharge voltage of approximately 9 kV at 10 mm confirmed the fit's validity. With this approach, the transition reduced electric field (E/N_{GS}) was calculated to be approximately 45 Td (based on a number density close to the Loschmidt constant). Notably, this value lies between the reduced electric field of the diffused discharge (~10 Td) and the reduced electric field of the spark discharge (~100 Td) (Fig. 3).

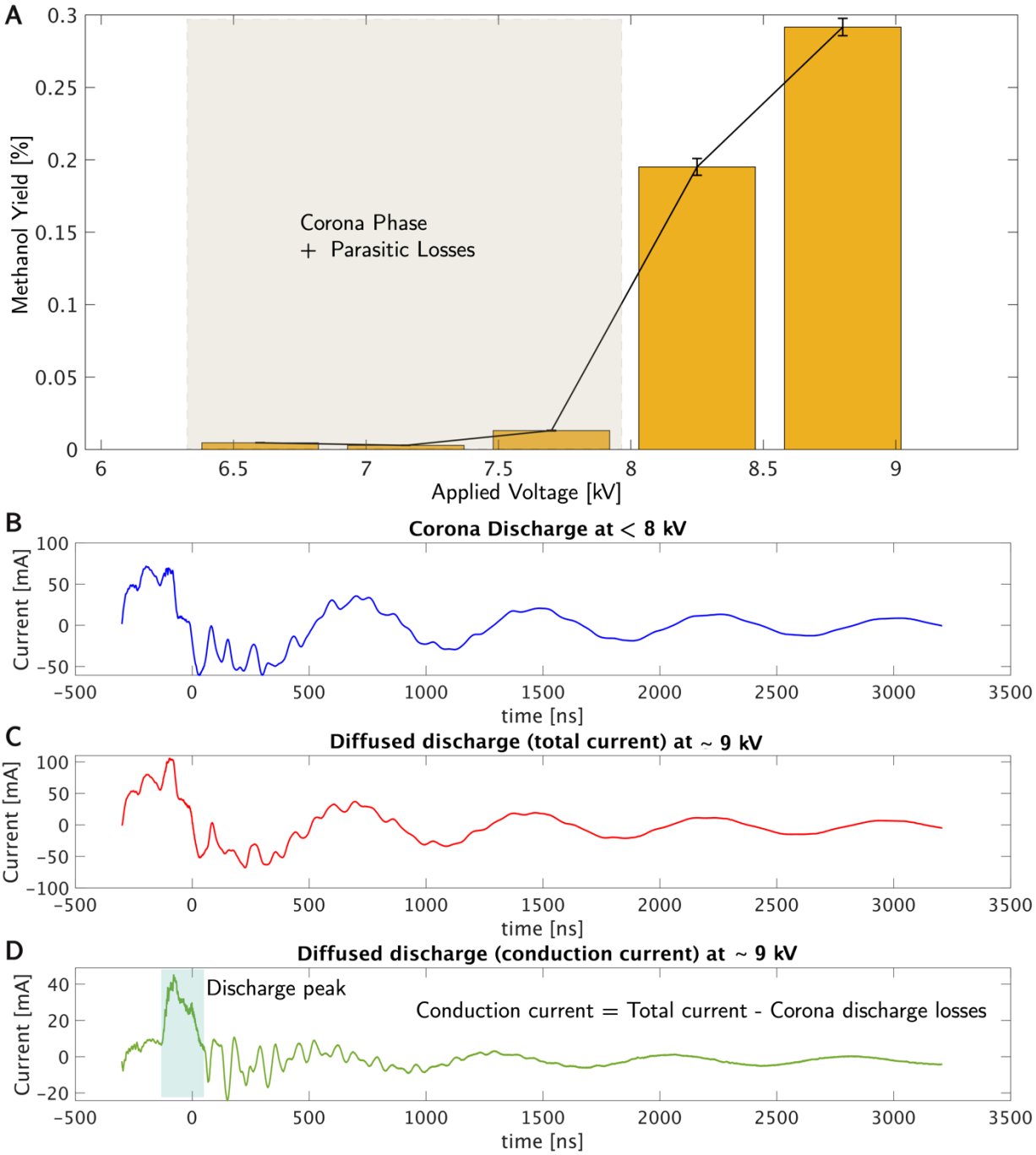

Fig. S16. Energy per pulse evaluation for longer discharge gaps (diffused discharge). (A) Methanol yield across plasma phases (discharge gap = 1 cm) showed that corona phase produced negligible amounts of methanol. The transition to discharges increased the yield of methanol by 10x. (B) Current waveform of the plasma in corona discharge regime averaged over 100 samples. (C) Current waveform of the plasma in diffused discharge regime (averaged over 100 samples) which is a combination of the discharge peak (conduction current peak) and corona discharge losses. (D) Conduction current [9] for the evaluation of energy per pulse at longer discharge gaps.

The energy deposited during the discharge was calculated by integrating the product of measured voltage and current waveforms over the duration highlighted in Fig. S16D. Later ringing periods reflect parasitic losses in our circuit and deposit negligible energy into the reactant molecules [9]. The total measured current (I_{total}) encompasses the conduction current (I_{cond}), and parasitic currents (I_{para}), which we have included losses due to corona,

$$I_{total} = I_{cond} + I_{para} \implies E_{total} = E_{plasma} + E_{corona} ,$$

where E_{total} is the total energy per pulse evaluated using the total current, E_{corona} is the corona energy losses, and E_{plasma} is the deposited discharge energy. The energy deposited per pulse was evaluated using the conduction current obtained by subtracting the current corresponding to corona and parasitic losses from the total current. This approach applies to the spark regime as well (Fig. S14).

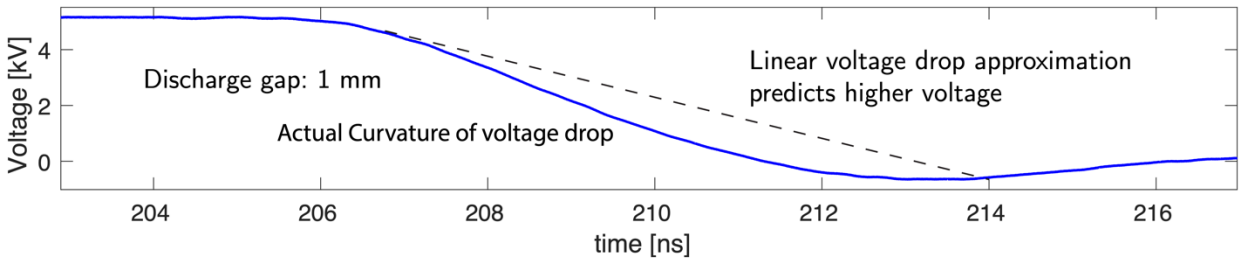

Fig. S17. Linear voltage profile approximation for longer discharge gaps.
Voltage waveform corresponding to a discharge gap of 1 mm to compare the actual voltage drop curvature (over discharge pulse width) with linear drop approximation.

The energy per pulse was evaluated for the diffused discharge using the glow-to-spark transition voltage (Fig. S15). Adding a voltage probe was found to load the circuit down eliminating the discharge (due to added capacitance. This issue was addressed using the theoretical peak discharge voltage predicted at 1 cm (Fig. S15) and taking a linear drop to zero over the plasma discharge period (defined as the pulse width of the discharge peak highlighted in Fig. S16D). This method estimated an upper bound of the energy deposited per pulse (as voltage drop is non-linear with concave upward curvature (Fig. S16E)) of ~ 23 μJ (Fig. S18A).

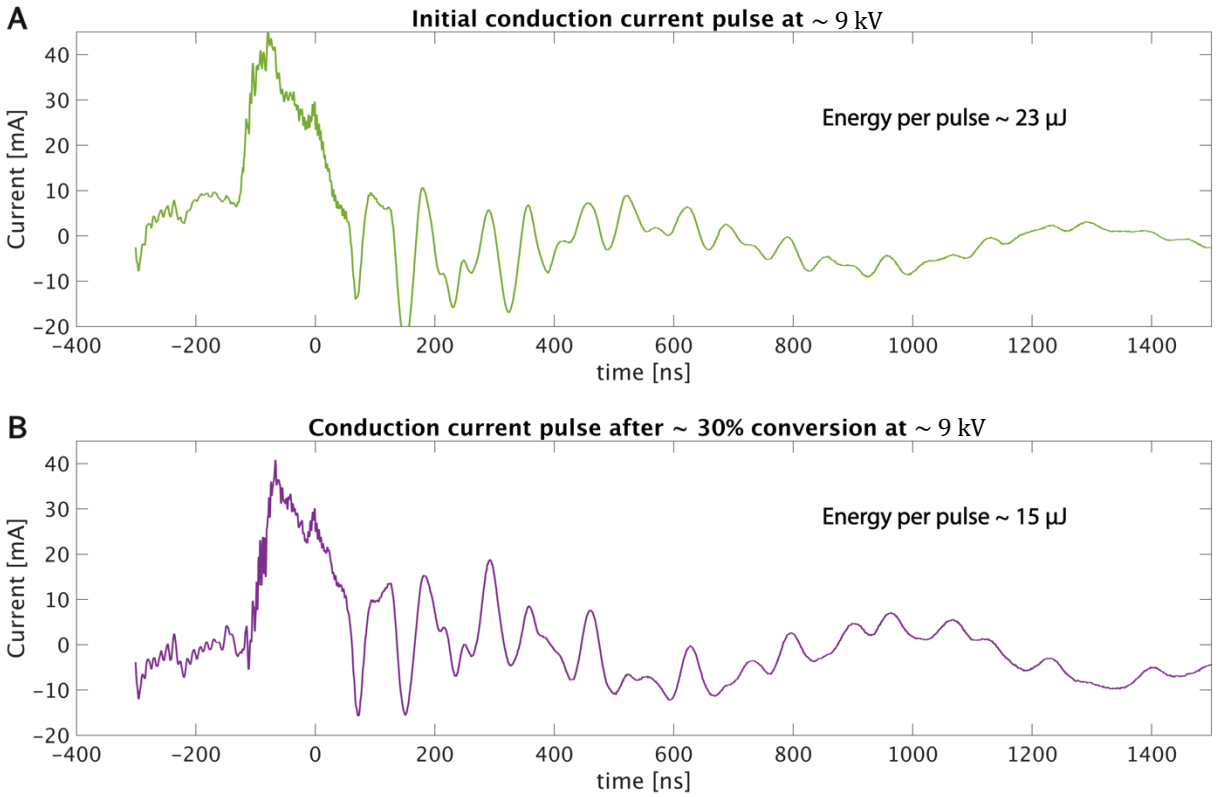

Fig. S18. Decrease in deposited energy per pulse with increasing reaction run time. (A) Conduction current at t = 0 (~ 0% conversion) with an energy deposited of ~ 23 µJ/pulse. (B) Conduction current at t ~ 100 min (~ 30% conversion) with an energy deposited of ~ 15 µJ/pulse.

With the increasing conversion in the reactor, the peak current and energy per pulse decreased. The results in Fig. 5 indicate methane conversions close to 80%, which suggests that the energy deposited per pulse would further decrease to around 3-4 µJ/pulse (estimated by linear extrapolation based on the drop from 0% to 30% conversion). Further verifying the energy drop, a ~ 100 µJ/pulse drop was observed on the input side of the nanosecond pulser over 30% conversion (Figs. S18-S19). Therefore, an average energy deposited per pulse (i.e., energy per pulse at 50% conversion) was chosen (~ 10 µJ/pulse). This energy is consistent with the upper end of reported values in the literature for diffused discharges [8,9]. Moreover, since the calculated energy is an upper bound (based on linear voltage drop, Fig. S16), it is reasonable to assume an average energy deposited per pulse of 10 µJ for the evaluation of specific energy input (SEI) in Fig. 5 corresponding to datapoints of 1 cm discharge gap.

11. Estimation of E/N ranges

E/N was estimated for different discharge regimes based on the applied voltage (V) and discharge gap (d) [8,10],

$$\text{Mean electric field (E)} = \frac{V - V_{cathode}}{d},$$

where $V_{cathode}$ represents cathode voltage drop or cathode fall voltage. N was assumed to be Loschmidt's constant [8]. Since the cathode voltage drop is ~ 0.2 kV [10] at 1 cm discharge gap, it was neglected (i.e., it is negligible compared to the applied voltage, ~ 9 kV). The mean electric field estimated using this approach for diffused and spark discharges falls in the typical range of electric fields reported in the literature [11,12].

For lower E/N range in Fig. 3C, the upper limit was chosen based on where methane dissociation starts.

12. Select reactions in plasma-assisted DMtM conversion

The DMtM mechanism (Fig. 3) combines prominent pathways where methane and oxygen are converted into products through plasma-mediated processes. This includes the excitation of reactants (i.e., vibrations) and generation of radicals (i.e., CH_3, H etc.). Reactions from the reaction mechanism (Fig. 3) are summarized in Table S1. These reactions are inferred from sensitivity analyses [13–15], stable products from GC chromatograms (Sec. 3), and energy loss fractions (Fig. 3C). The presence of key intermediates (e.g., O, H, CH, etc.) were confirmed with OES measurements.

Table S1. List of reactions used in the DMtM mechanism (Fig. 3).

High E/N reactions	***Low E/N reactions***
$e^- + CH_4 \rightarrow CH_3 + H + e^-$	$e^- + CH_4 \rightarrow CH_4^{\nu} + e^-$
$e^- + O_2 \rightarrow O + O + e^-$	$e^- + O_2 \rightarrow O_2^{\nu} \rightarrow O + O + e^-$
$O + H \rightarrow OH$	$e^- + O_2 \rightarrow O + O + e^-$
$CH_3 + O \rightarrow CH_3O$	$CH_4^{\nu} + O \rightarrow CH_3O + H$
$H + OH \rightarrow H_2O$	$O + H \rightarrow OH$
$H + H \rightarrow H_2$	$OH + H \rightarrow H_2O$
$CH_3 + CH_3 \rightarrow C_2H_6$	$H + H \rightarrow H_2$
$CH_3 + OH \rightarrow CH_3OH$	$CH_3O + H \rightarrow CH_3OH$
$CH_3O + H \rightarrow CH_3OH$	$CH_3O + CH_3O \rightarrow CH_3OH + HCHO$
$CH_3OH + OH \rightarrow CH_2OH + H_2O$	$CH_3OH + OH \rightarrow CH_2OH + H_2O$
$CH_2OH + O \rightarrow HCHO + OH$	$CH_2OH + O \rightarrow HCHO + OH$
$HCHO + OH \rightarrow HCO + H_2O$	$HCHO + OH \rightarrow HCO + H_2O$
$CH_2OH + CH_3 \rightarrow CH_3CH_2OH$	$HCO + OH \rightarrow HCOOH$
$HCO + CH_3 \rightarrow CH_3CHO$	$HCO + O_2 \rightarrow CO + HO_2$
$CH_3CHO + CH_3 \rightarrow CH_3COCH_3 + H$	$CO + OH \rightarrow CO_2 + H$
$CH_3CHO + OH \rightarrow CH_3COOH + H$	$CO_2 + O \rightarrow CO + O_2$
$HCO + OH \rightarrow HCOOH$	
$HCO + O_2 \rightarrow CO + HO_2$	
$CO + OH \rightarrow CO_2 + H$	
$CO_2 + O \rightarrow CO + O_2$	
$CH_3 \rightarrow CH + H + H$	
$CH \rightarrow C + H$	
$C + C \rightarrow C_2$	

13. 95% confidence intervals for estimated rate constants

Table S2. 95% confidence intervals for rate constants in Fig. 2.

Energy per pulse (μJ/pulse)	Parameter name	Parameter value (min^{-1})	95% Confidence Interval (min^{-1})
10	$k_1 + k_3$	2.4×10^{-3}	$2.3 \times 10^{-3} – 2.5 \times 10^{-3}$
	k_1	2.5×10^{-4}	$2.2 \times 10^{-4} – 2.7 \times 10^{-4}$
	k_2	3.2×10^{-2}	$2.8 \times 10^{-2} – 3.6 \times 10^{-2}$
40	$k_1 + k_3$	2.1×10^{-2}	$1.9 \times 10^{-2} – 2.3 \times 10^{-2}$
	k_1	7.0×10^{-4}	$6.2 \times 10^{-4} – 7.8 \times 10^{-4}$
	k_2	1.4×10^{-1}	0.1 – 0.2

Table S3. 95% confidence intervals for rate constants in Fig. 4.

Damköhler number	Parameter name	Parameter value (min^{-1})	95% Confidence Interval (min^{-1})
0.1	$k_1 + k_3$	2.4×10^{-3}	$2.4 \times 10^{-3} – 2.5 \times 10^{-3}$
	k_1	6.7×10^{-4}	$0 – 2.0 \times 10^{-3}$
	k_2	3.3×10^{-14}	0 – 0.2
	k_4	1.1×10^{-1}	$0 – 2.2 \times 10^{-1}$
0.2	$k_1 + k_3$	1.8×10^{-3}	$1.7 \times 10^{-3} – 1.9 \times 10^{-3}$
	k_1	2.6×10^{-4}	$0 – 7.9 \times 10^{-4}$
	k_2	3.9×10^{-12}	0 – 0.1
	k_4	5.0×10^{-2}	$0 – 1.0 \times 10^{-1}$

Kinetic models (Sec. 1) were fit to experimental data from Fig. 2 and 4 in the main text. The $k_1 + k_3$ parameter was extracted from CH_4 conversion first and used in subsequent fits of CH_3OH yield. Confidence intervals of these fits are demonstrated in Table S2-S3.

14. Input energy cost

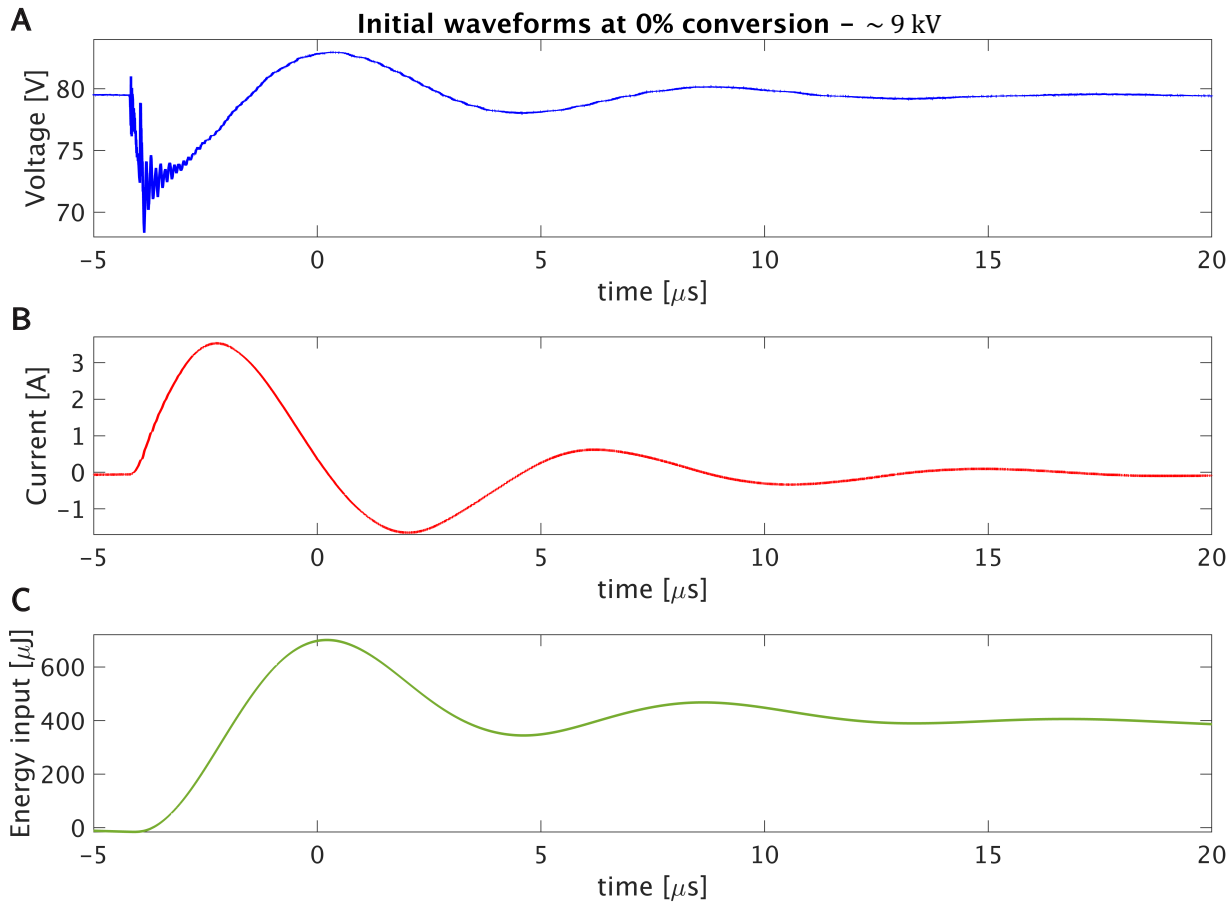

Fig. S19. Input energy to the nanosecond pulser at 0% conversion.
(A) Input voltage waveform from DC supply (Materials and Methods) to the nanosecond pulser at t = 0 (or 0% conversion). The discharge gap was 1 cm at the output side of the pulser. (B) Input current waveform at the same settings. (C) Total energy input as a function of time obtained by integrating the product of voltage and current.

The total energy input was evaluated by integrating the product of applied voltage (Fig. S19A) and current (Fig. S19B) over 20 μs (beyond which energy change flattens). The total energy input at 20 μs was ~ 390 μJ while the energy deposited during the discharge phase (i.e., when methanol is formed) was ~ 20 μJ. This discrepancy includes inefficiencies of the voltage amplifier, its energy penalty, corona losses, and parasitic losses.

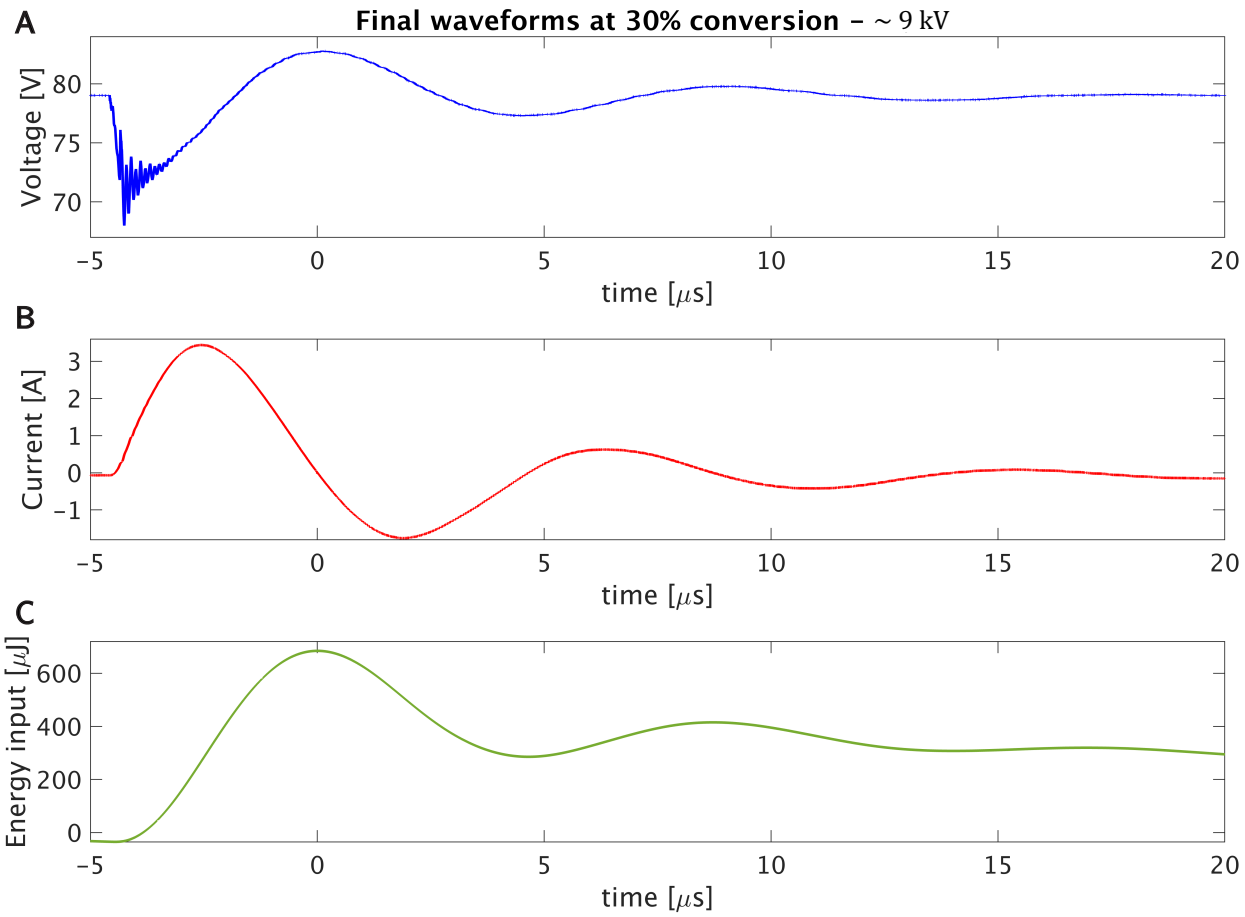

Fig. S20. Input energy to the nanosecond pulser at 30% conversion.
(A) Input voltage waveform from DC supply (Materials and Methods) to the nanosecond pulser at ~ 30% conversion. The discharge gap was 1 cm at the output side of the pulser. (B) Input current waveform at the same settings. (C) Total energy input as a function of time obtained by integrating the product of voltage and current.

The total energy input at 30% conversion was ~ 295 μJ. This is ~ 100 μJ lower than the energy cost at 0% conversion.

15. Emission spectra of filamentary and diffused discharges

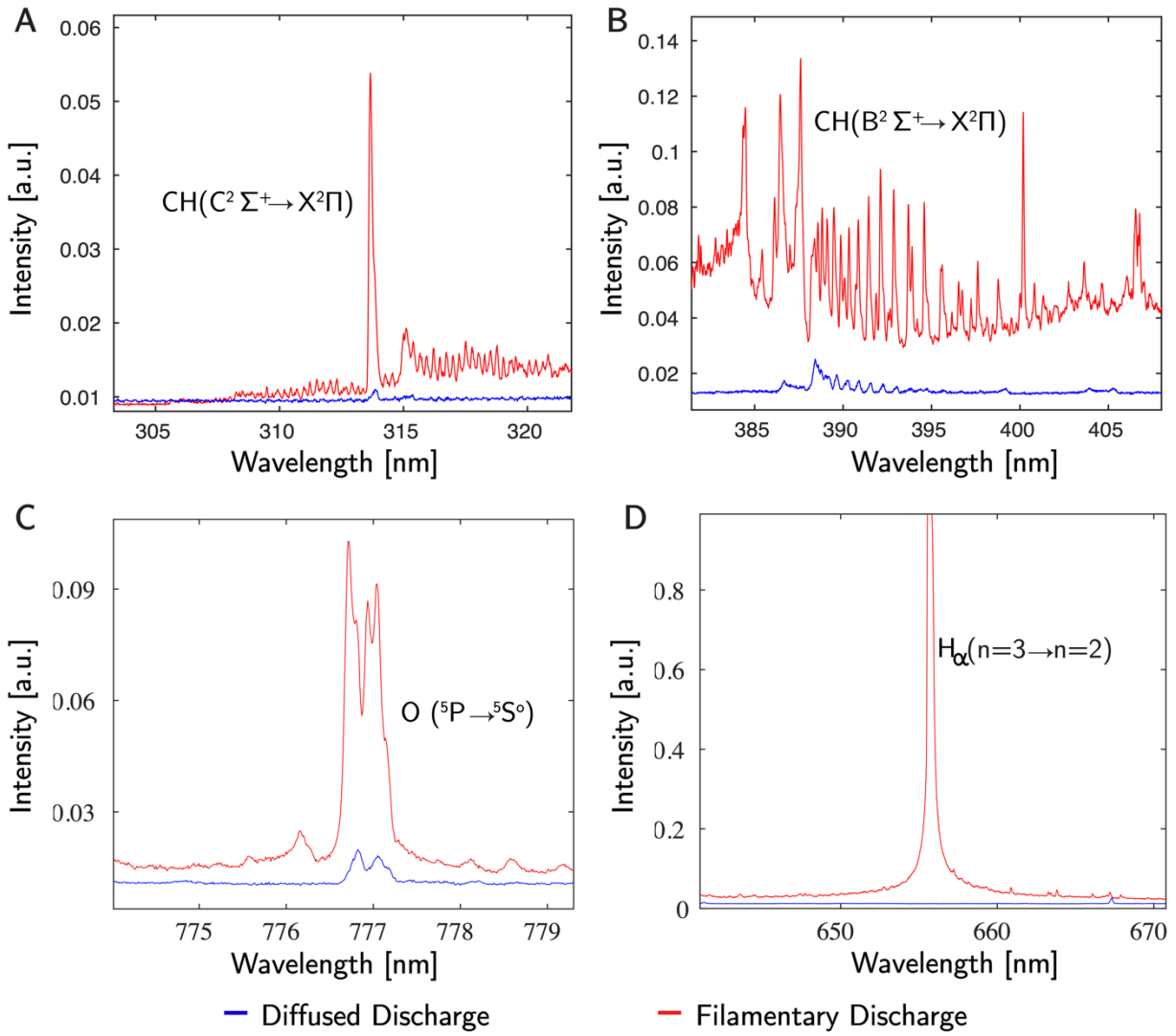

Fig. S21. Emission spectra of various species in filamentary and diffused discharges. (A) Huge intensity difference between filamentary and diffused discharges for higher energy CH bands CH (C → X) and (B) Emission band of CH (B → X). (C) O emission triplet from both filamentary and diffused discharges. (D) H_α peak present only in filamentary discharge.

16. Influence of cold water-bath and pump circulation on methanol yield

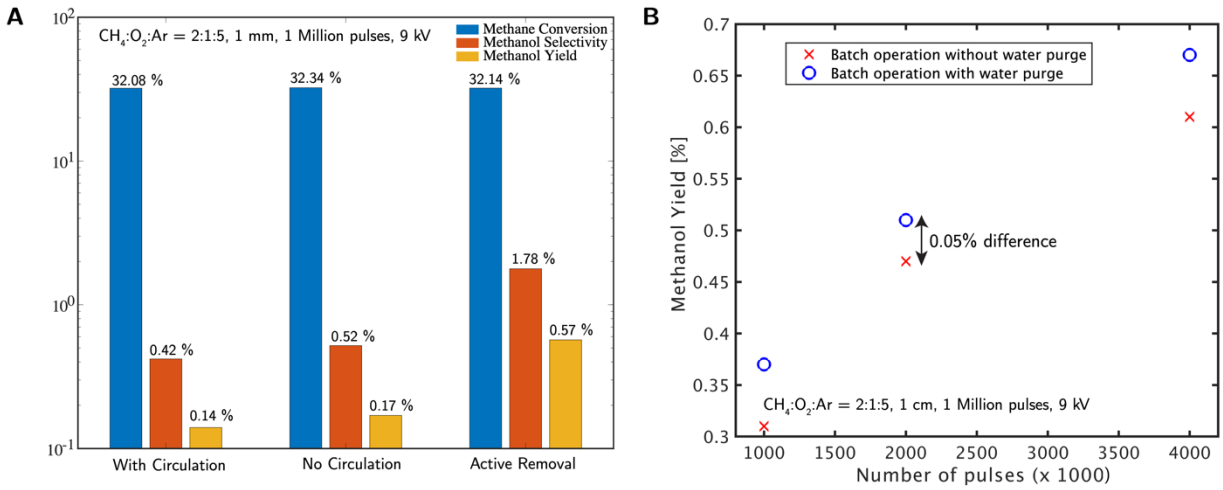

Fig. S22. Influence of pump circulation and water purging on methanol yield.
(A) A difference of < 0.05% in methanol yield with and without circulation and a 3-fold improvement with water and circulation showing pure circulation without capturing methanol does not lead to improvement in methanol yield, and (B) a difference of 0.05% in methanol yield showing water purging alone cannot show the improvement in methanol yields shown in Fig. 4 in the manuscript.

As circulation of reactants and products using a pump in a closed loop system can change the temperature of the reactor walls, we performed experiments with species circulation and without circulation to segregate methanol yield improvement via active removal strategy as proposed in Fig. 4. We showed that there is only < 0.05% difference in methanol yield between circulation and no circulation, and therefore circulation alone cannot be the reason for 3-fold improvement in methanol yield with active phase removal.

Similarly, having initial gas purge of the batch reactor in the presence of cold water-bath only showed a difference of 0.05% in methanol yield. Therefore, reactor temperature change due to cold-water bath alone cannot explain the performance improvement from < 1% methanol yield to 21.4% demonstrated in Fig. 4.

References:

(1) Pai, D. Z.; Stancu, G. D.; Lacoste, D. A.; Laux, C. O. Nanosecond Repetitively Pulsed Discharges in Air at Atmospheric Pressure—the Glow Regime. *Plasma Sources Sci Technol* **2009**, *18* (4), 045030. https://doi.org/10.1088/0963-0252/18/4/045030.

(2) Castela, M.; Stepanyan, S.; Fiorina, B.; Coussement, A.; Gicquel, O.; Darabiha, N.; Laux, C. O. A 3-D DNS and Experimental Study of the Effect of the Recirculating Flow Pattern inside a Reactive Kernel Produced by Nanosecond Plasma Discharges in a Methane-Air Mixture. *Proceedings of the Combustion Institute* **2017**, *36* (3), 4095–4103. https://doi.org/10.1016/J.PROCI.2016.06.174.

(3) Yardley, J. T, Moore, C. B. Vibration→Vibration and Vibration→Translation Energy Transfer in Methane-Oxygen Mixtures. *J Chem Phys* **1968**, *48* (1), 14–17. https://doi.org/10.1063/1.1664460.

(4) Tyuterev, V.; Tashkun, S.; Rey, M.; Kochanov, R.; Nikitin, A.; Delahaye, T. Accurate Spectroscopic Models for Methane Polyads Derived from a Potential Energy Surface Using High-Order Contact Transformations. *Journal of Physical Chemistry A* **2013**, *117* (50), 13779–13805. https://doi.org/10.1021/JP408116J/SUPPL_FILE/JP408116J_SI_001.ZIP.

(5) Hess, P.; Moore, C. B. Vibrational Energy Transfer in Methane and Methane–Rare-gas Mixtures. *J Chem Phys* **1976**, *65* (6), 2339–2344. https://doi.org/10.1063/1.433346.

(6) Butterworth, T.; Van De Steeg, A.; Van Den Bekerom, D.; Minea, T.; Righart, T.; Ong, Q.; Van Rooij, G. Plasma Induced Vibrational Excitation of CH4—a Window to Its Mode Selective Processing. *Plasma Sources Sci Technol* **2020**, *29* (9), 095007. https://doi.org/10.1088/1361-6595/ABA1C9.

(7) De Vasconcelos, M. H.; De Vries, A. E. Vibrational Relaxation Time Measurements in CH4 and CH4-Rare Gas Mixtures. *Physica A: Statistical Mechanics and its Applications* **1977**, *86* (3), 490–512. https://doi.org/10.1016/0378-4371(77)90091-7.

(8) Pai, D. Z.; Lacoste, D. A.; Laux, C. O. Transitions between Corona, Glow, and Spark Regimes of Nanosecond Repetitively Pulsed Discharges in Air at Atmospheric Pressure. *J Appl Phys* **2010**, *107* (9), 93303. https://doi.org/10.1063/1.3309758/388505.

(9) Pai, D.; Lacoste, D. A.; Laux, C. O. Nanosecond Repetitively Pulsed Plasmas in Preheated Air at Atmospheric Pressure - The Diffuse Regime. *39th AIAA Plasmadynamics and Lasers Conference* **2008**. https://doi.org/10.2514/6.2008-4091.

(10) Naidis, G. V. Simulation of Streamer-to-Spark Transition in Short Non-Uniform Air Gaps. *J. Phys. D: Appl. Phys* **1999**, *32*, 2649–2654.

(11) Starikovskaia, S. M. Plasma Assisted Ignition and Combustion. *J. Phys. D: Appl. Phys* **2006**, *39*, 265–299. https://doi.org/10.1088/0022-3727/39/16/R01.

(12) Shao, T.; Wang, R.; Zhang, C.; Yan, P. Atmospheric-Pressure Pulsed Discharges and Plasmas: Mechanism, Characteristics and Applications. *High Voltage* **2018**, *3* (1), 14–20. https://doi.org/10.1049/HVE.2016.0014.

(13) Sun, J.; Chen, Q.; Yang, X.; Koel, B. E. Effects of Non-Equilibrium Excitation on Methane Oxidation in a Low-Temperature RF Discharge. *J. Phys. D: Appl. Phys* **2020**, *53*, 13. https://doi.org/10.1088/1361-6463/ab57dc.

(14) Sun, W.; Uddi, M.; Won, S. H.; Ombrello, T.; Carter, C.; Ju, Y. Kinetic Effects of Non-Equilibrium Plasma-Assisted Methane Oxidation on Diffusion Flame Extinction Limits.

Combust Flame **2012**, *159* (1), 221–229. https://doi.org/10.1016/J.COMBUSTFLAME.2011.07.008.

(15) Indarto, A.; Choi, J. W.; Lee, H.; Song, H. K. The Kinetic Studies of Direct Methane Oxidation to Methanol in the Plasma Process. *Chinese Science Bulletin* **2008**, *53* (18), 2783–2792. https://doi.org/10.1007/S11434-008-0384-4/METRICS.